ADVANCED FUNCTIONAL MATERIALS
www.afm-journal.de

Electrochemical Mg^{2+} Displacement Driven Reversible Copper Extrusion/Intrusion Reactions for High-Rate Rechargeable Magnesium Batteries

*Xiaolan Xue, Renpeng Chen, Xinmei Song, Anyang Tao, Wen Yan, Weihua Kong, and Zhong Jin**

Rechargeable magnesium batteries (RMBs) based on metal Mg anodes have shown great potential owing to the abundant natural resources, high volumetric capacity, and low safety hazard. Nevertheless, the development of RMBs is hampered by the sluggish kinetics of Mg^{2+} diffusion and the limited cyclability of cathode materials. Herein, nonstoichiometric copper selenide ($Cu_{2-x}Se$) are synthesized via a solution-based method and exploited as a durable cathode material based on ionic displacement mechanism for RMBs. The copper ions in the Se^{2-} based sub-lattices are reversibly exchanged by Mg^{2+} ions without causing lattice collapse. Owing to the same face-centered cubic Se^{2-} sub-lattices and similar unit cell size of $Cu_{2-x}Se$ and MgSe, the energy barrier for lattice reconstruction during cycling processes is very low, significantly improving the rate performance, structural stability, and cycle life of the $Cu_{2-x}Se$ cathode. Moreover, metal Cu is in situ generated during discharging, thus greatly facilitating electron transport. Comprehensive characterizations confirm that the $Cu_{2-x}Se$ cathode undergoes reversible copper ion extrusion/reinjection during the discharge–charge steps. This work suggests the great potential for exploring high-performance electrode materials based on ionic displacement mechanism for advanced multivalent-ion secondary batteries.

1. Introduction

To alleviate the intensified energy and environment crisis, the development of sustainable energy storage technologies is imperative. Commercial lithium ion batteries (LIBs) suffer from the limited lithium resource and the safety issues caused by Li dendritic growth during cycling processes.[1,2] Recently, extensive research interests have been focused on developing post-LIBs energy storage systems with low cost and good sustainability, including sodium-ion batteries,[3] potassium-ion batteries,[4] and multivalent ion batteries (e.g., rechargeable magnesium batteries (RMBs), zinc-ion batteries, and aluminum-ion batteries).[5–8] Among them, RMBs based on metal Mg anodes have drawn increasing attention because of the high natural abundance, high theoretical specific capacity (volumetric capacity 3833 mAh mL^{-1}, gravimetric capacity 2205 mAh g^{-1}), and good safety.[8,9] Unfortunately, the limited choices of cathode materials with fast kinetics and good durability severely hinder the development of RMBs.[10] One major reason is that the large charge/radius ratio and high polarization of Mg^{2+} cations result in strong electrostatic interaction between Mg^{2+} and the anions in cathode lattices, greatly lowering the insertion and diffusion kinetics of Mg^{2+} ions.[11,12] The reported cathode materials applied to RMBs are mainly based on intercalation or conversion mechanisms, including elemental sulfur, transition metal oxides, sulfides, selenides, etc.[13–18] However, the rate capability and cycling stability of the cathode materials are still to be further improved.

Transition metal selenides have "softer" anion lattices than oxides and sulfides, and the Coulombic interaction between Se^{2-} lattices and guest Mg^{2+} ions is much weaker than those of O^{2-} and S^{2-} lattices. Therefore, it is proposed that the selenides have great potential to serve as the hosts for Mg^{2+} cations. On the other hand, copper sulfide and selenide were found to be fast ion conductors with unique physiochemical properties.[19,20] This is because the copper cations exhibit relatively high mobility in the stable face-centered cubic (fcc) S^{2-} or Se^{2-} sub-lattices, thus conducive to promoting the displacement by other guest cations without the reconstruction of anion lattices. However, the magnesium storage behavior of $Cu_{2-x}Se$ is still unclear and need to be explored. In this work, we prepared nonstoichiometric cubic-phase $Cu_{2-x}Se$ nanoplates by a convenient solution-based method, and explored their electrochemical performance and intrinsic mechanism as a Mg^{2+} host material. Various ex situ characterizations, including X-ray powder diffraction (XRD), X-ray photoelectron spectroscopy (XPS),

Dr. X. L. Xue, Dr. R. P. Chen, X. M. Song, A. Y. Tao, W. Yan, W. H. Kong, Prof. Z. Jin
Key Laboratory of Mesoscopic Chemistry of MOE
School of Chemistry and Chemical Engineering
Nanjing University
Nanjing, Jiangsu 210023, China
E-mail: zhongjin@nju.edu.cn

The ORCID identification number(s) for the author(s) of this article can be found under https://doi.org/10.1002/adfm.202009394.

DOI: 10.1002/adfm.202009394

high-resolution transmission electron microscopy (HRTEM), energy dispersive X-ray spectroscopy (EDX), and inductively coupled plasma optical emission spectroscopy (ICP-OES) were conducted, verifying that the $Cu_{2-x}Se$ cathode reacted with Mg^{2+} cations through an ionic displacement mechanism. The Mg^{2+} displacement reaction and copper ion intrusion/extrusion processes were rapidly proceeded along with the good maintenance of Se^{2-} anion frameworks, in favor of the structure integrity and capacity retention of $Cu_{2-x}Se$ cathode. The reversible copper ion intrusion/extrusion made the $Cu_{2-x}Se$ cathode less vulnerable to lattice structure collapse. Notably, it was found that metal Cu was in situ formed by ionic displacement during the discharge steps, greatly enhancing the conductivity and facilitating charge transport. Benefiting from these merits, the RMBs based on $Cu_{2-x}Se$ cathodes exhibit high rate performance (222 mAh g^{-1} at 100 mA g^{-1} and 155 mAh g^{-1} at 1000 mA g^{-1}) and long-term cyclability (with a capacity retention of ≈84.3% even after 500 cycles at 1000 mA g^{-1}).

2. Results and Discussion

The $Cu_{2-x}Se$ nanoplates were successfully synthesized via a one-step reaction process in a diethylenetriamine (DETA)-water mixture based solvothermal system. The morphology and structure of $Cu_{2-x}Se$ nanoplates were investigated by SEM, TEM, and HRTEM characterizations. As presented in **Figure 1**a,b, the $Cu_{2-x}Se$ product consisted of stacked hexagonal nanoplates (0.5–2 µm in diameter and 10–20 nm in thickness), accompanied with some small $Cu_{2-x}Se$ nanoparticles. The HRTEM image (Figure 1c) shows distinct lattice fringes with an interplanar spacing of 0.332 nm, corresponding to the (111) plane of cubic-phase $Cu_{2-x}Se$. The inset in Figure 1c displays the corresponding fast Fourier transform (FFT) pattern, demonstrating the single-crystalline characteristics of $Cu_{2-x}Se$. Energy dispersive X-ray spectroscopy (EDX) elemental mappings indicate that the Cu and Se atoms are uniformly distributed in $Cu_{2-x}Se$ nanoplates (Figure 1d–f). All the peaks in the XRD pattern of $Cu_{2-x}Se$ nanoplates (Figure 1g) can be well assigned to cubic-phase $Cu_{2-x}Se$ (JCPDS no. 06–0680), and no impurity peaks are observed. The Raman spectrum (Figure S1, Supporting Information) shows a strong peak located at 258.9 cm^{-1} originated from the stretching vibration of Se–Se bonds.[21] XPS analysis (Figure S2, Supporting Information) were used to identify the compositions and chemical states of the elements in $Cu_{2-x}Se$ nanoplates, confirming the presence of Cu and Se elements. The high-resolution XPS spectra of Cu 2p and Se 3d are provided in Figure 1h,i. The two strong peaks in Cu 2p spectrum (Figure 1h) can be deconvoluted at 932.35 and 952.23 eV originated from Cu $2p_{3/2}$ and Cu $2p_{1/2}$ bands of Cu^{+} species; the two weak peaks at 934.1 and 954.35 eV are derived from Cu $2p_{3/2}$ and Cu $2p_{1/2}$ bands of Cu^{2+} species; the two characteristic

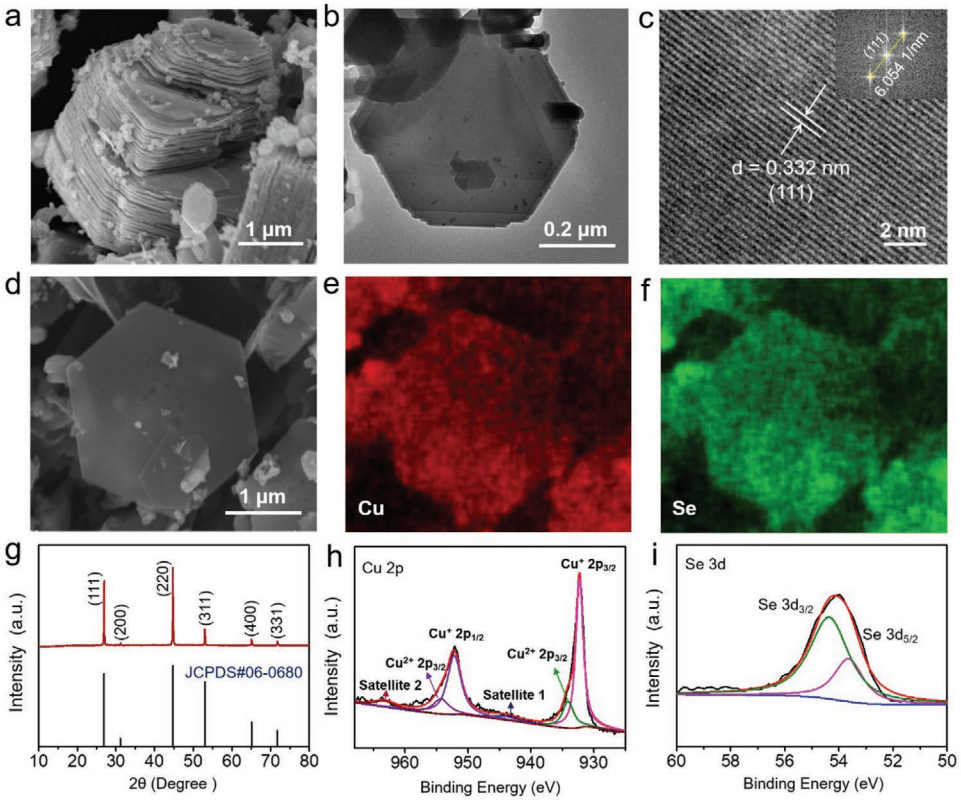

Figure 1. Structural and compositional characterizations of cubic-phase $Cu_{2-x}Se$ (berzelianite) nanoplates. a) SEM, b) TEM, and c) HRTEM images of $Cu_{2-x}Se$ nanoplates. The inset in c) is the corresponding fast Fourier transform (FFT) pattern. d–e) SEM image and corresponding energy dispersive X-ray spectroscopy (EDX) elemental mappings of $Cu_{2-x}Se$ nanoplates. g) X-ray powder diffraction (XRD) pattern and h,i) X-ray photoelectron spectroscopy (XPS) spectra at the h) Cu 2p and i) Se 3d energy levels of $Cu_{2-x}Se$ nanoplates.

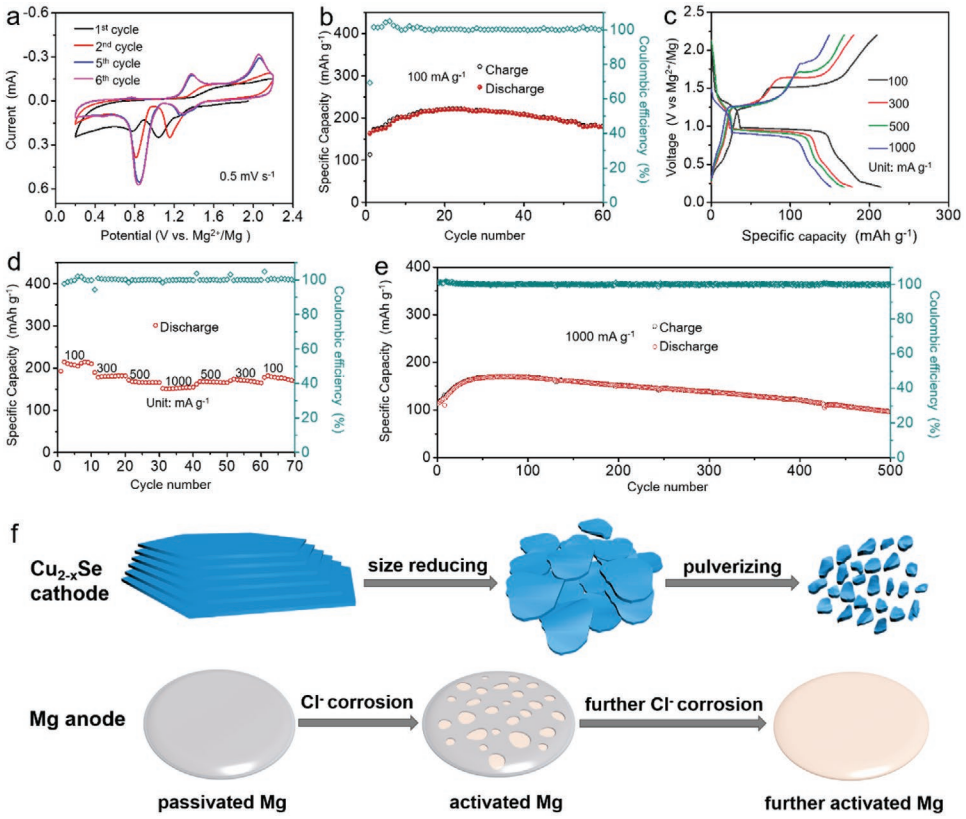

Figure 2. Magnesium storage performance of $Cu_{2-x}Se$ electrode. a) Cyclic voltammetry (CV) curves at a scan rate of 0.5 mV s^{-1} in the voltage range of 0.2–2.2 V (versus Mg^{2+}/Mg). b) Cycling performance at the current density of 100 mA g^{-1}. c) Galvanostatic discharge–charge profiles at the different current densities. d) Rate capability profiles obtained at various current densities of 100, 300, 500, and 1000 mA g^{-1}, respectively. e) Long-term cycling performance at a high current density of 1000 mA g^{-1}. f) Proposed schematic explanation for the activation and capacity decay processes of $Cu_{2-x}Se$ based rechargeable magnesium batteries (RMBs).

satellite peaks at 943.6 and 962.35 eV are derived from Cu^{2+} species.[22,23] The atomic ratio of Cu^{+} to Cu^{2+} in the prepared sample calculated from their peak areas is 2.4:1. The content of Cu^{2+} is relatively high, possibly owing to the slight surface oxidation of the sample. In the Se 3d spectrum (Figure 1i), the two peaks located at 53.7 and 54.4 eV are ascribed to the Se $3d_{5/2}$ and Se $3d_{3/2}$ bands of Se^{2-} species, respectively.[24]

To avoid the corrosion of electrolyte to current collector and battery case, Mo foil as the current collector with high electrochemical stability is placed underneath the $Cu_{2-x}Se$ cathode. As shown in Figure S3 (Supporting Information), the Mg plating/stripping efficiency on Mo foil is near 100% after an activation process, indicating that the electrolyte does not corrode the Mo foil current collector and battery case. The electrochemical performance of $Cu_{2-x}Se$ nanoplates as cathode material in RMBs based on nonaqueous electrolyte was investigated by cyclic voltammetry (CV) and galvanostatic discharge–charge processes (**Figure 2**). Figure 2a presents the CV curves of $Cu_{2-x}Se$ cathode under a sweep rate of 0.5 mV s^{-1} in the potential range of 0.2–2.2 V (versus Mg^{2+}/Mg). It is worth noting that the CV peaks in the first cycle is obviously different from those in the following cycles. Compared to the initial cycle, the reduction peaks during the subsequent cycles shift to more positive potentials, while the oxidation peaks shift to more negative potentials. This may be due to the possible presence of $Cu_{2-x}O$ surface oxidation layer or adsorbed residual organic amine species on the $Cu_{2-x}Se$ surface, leading to a surface activation process of the $Cu_{2-x}Se$ cathode during the first cycle.[25] This irreversible process decreases the Coulomb efficiency in the first cycle, and makes the shape of the CV curve in the first cycle significantly different from those in the subsequent cycles. As the cycling proceeds, the current values of the reduction peak at ≈0.85 V and the oxidation peaks (at ≈1.37 and ≈2.0 V) show notable improvements, indicating the cathode undergoes an activation process during the discharge–charge processes. Since the fifth cycle, the latter CV curves are well overlapped, suggesting the good reversibility after the activation process.

Figure 2b displays the cycling performance of $Cu_{2-x}Se$ cathode at 100 mA g^{-1}. The discharge and charge capacities at the first cycle are 113 and 163 mAh g^{-1}, respectively. After about 25 cycles, the discharge capacity reaches a high value of 222 mAh g^{-1}, and the Coulombic efficiency keeps at nearly 100%. The reversible discharge capacity of $Cu_{2-x}Se$ cathode after 60 cycles still maintains at 179 mAh g^{-1}, indicating the good cycling stability. The Coulombic efficiency of the first 10 cycles in Figure 2b is higher than 100%, which should be ascribed to the self-discharge phenomenon and some side reactions (e.g., the reaction between residual amine in the active material and electrolyte). This similar phenomenon has also been reported in other previous works.[26,27] The galvanostatic

discharge–charge profiles (Figure S4, Supporting Information) show two discharge plateaus at around 1.35 and 0.95 V and two charge plateaus at around 1.30 and 1.50 V, corresponding to the two-step magnesiation–demagnesiation processes, respectively, which are in good agreement with the above CV results. Moreover, the $Cu_{2-x}Se$ cathode exhibits an excellent rare performance, as presented in Figure 2c. When the current densities increase from 100 to 1000 mA g^{-1}, the discharge–charge profiles show well maintained voltage plateaus and capacity retention, revealing the low electrochemical polarization of $Cu_{2-x}Se$ electrode. The voltage hysteresis of ≈0.35 V at 1000 mA g^{-1} is much lower than the values in most of the previous reports, conducive to the improvement of energy efficiency of the RMB system.[28] The $Cu_{2-x}Se$ cathode delivers specific discharge capacities of 214, 182, 166, and 155 mAh g^{-1} at 100, 300, 500, and 1000 mA g^{-1}, respectively, demonstrating the excellent rate capability (Figure 2d). The Coulombic efficiency keeps at almost 100% during the rate test, suggesting the highly reversible magnesiation–demagnesiation processes. When the current density gradually decreases back to 100 mA g^{-1}, a discharge capacity of 182 mAh g^{-1} is still achieved, indicating the good electrochemical stability of $Cu_{2-x}Se$ cathode at high current rates. Long cycling performance at the high current density of 1000 mA g^{-1} was also evaluated. Figure 2e displays that the $Cu_{2-x}Se$ cathode exhibits an initial discharge specific capacity of 115 mAh g^{-1} and reaches a maximum capacity of 170 mAh g^{-1} at the 70th cycle after the gradual activation of the cathode.[29,30] The discharge capacity still maintains at 97 mAh g^{-1} after 500 cycles, which is ≈84.3% of the initial value. Moreover, the Coulombic efficiency is kept at ≈100% during the entire cycling process. Notably, the activation cycle number at high current density is higher than that at low current density. This is because that the longer discharge–charge reaction time at low current density can provide sufficient time for the consumption of impurities, leading to the fewer activation cycles.

It is notable that the $Cu_{2-x}Se$ cathode undergoes a long activation process during the discharge–charge tests. This phenomenon is probably owing to the surface activation and size reduction of $Cu_{2-x}Se$ nanoplates can facilitate the diffusion of Mg^{2+} ions and improve the utilization ratio of active material,[31] as illustrated in Figure 2f. In addition, the Cl^- ions in the non-nucleophilic electrolyte based on bis(hexamethyldisilazido) magnesium ($Mg(HMDS)_2$) and $AlCl_3$ can etch off the oxide passivation layer on metal Mg anode to activate the Mg surface, further leading to the capacity enhancement.[32] To demonstrate that Cl^- ions can activate the passivated Mg foil, CV tests were carried out with Pt foil as working electrode and Mg foil as both reference and counter electrodes. As displayed in Figure S5a (Supporting Information), with the increase of the CV cycle numbers, both the Mg plating/stripping current and the Coulombic efficiency obviously increase, indicating that the Mg plating/stripping in the electrolyte has undergone an activation process. Moreover, the Mg plating/stripping overpotential of Mg–Mg symmetric cell at 0.20 mA cm^{-2} decreases gradually in the first 50 cycles, also indicating that the cell has undergone an activation process (Figure S5b, Supporting Information). The above results confirm that the activation process originated from the corrosion of Cl^- ions in the electrolyte to Mg anode. However, as the active material is further pulverized, the capacity will start to decrease, owing to the degradation of Se^{2-} anion sub-lattices. The TEM images in Figure S6 (Supporting Information) shows the morphologies of $Cu_{2-x}Se$ cathode after 100 and 500 cycles at 1000 mA g^{-1}, respectively. It is observed that the size of $Cu_{2-x}Se$ nanoplates decreases with the increase of cycle numbers. Electrochemical impedance spectroscopy (EIS) was conducted to investigate the electrochemical kinetics of $Cu_{2-x}Se$ cathode. As presented in Figure S7a (Supporting Information), the Nyquist plot of the pristine $Cu_{2-x}Se$ cathode displays two semicircles in the high frequency region, corresponding to the charge transfer resistance (R_{ct}) of the cathode and anode, respectively. The high R_{ct} is mainly ascribed to the slow electrochemical reaction kinetics caused by the high polarization of Mg^{2+} and complex electrolyte system. After the activation for 10 cycles at 100 mA g^{-1}, the $Cu_{2-x}Se$ electrode at both fully charged and discharged states shows smaller R_{ct} compared to the pristine $Cu_{2-x}Se$ electrode, which is in accordance with the CV results and can be regarded as a good explanation for the activation process. Moreover, the R_{ct} of $Cu_{2-x}Se$ electrode at fully discharged state is smaller than that at fully charged state (Figure S7b, Supporting Information), manifesting the enhanced conductivity resulted from the in situ formation of metal Cu during discharging (as verified below).

A serious of ex situ characterization methods are used to clarify the magnesium storage mechanism of the $Cu_{2-x}Se$ cathode (**Figure 3**, Figure S8 and Table S1, Supporting Information). The XRD patterns of the pristine carbon paper (CP) and the as-prepared pristine $Cu_{2-x}Se$ electrode (stage A) were firstly collected (Figure 3a,b). After discharged to 1.05 V versus Mg^{2+}/Mg (stage B), the new diffraction peaks appeared at 12.8° and 36.5° are derived from orthorhombic Cu_2Se_y, which is an intermediate discharge product; meanwhile, three new peaks emerged at 28.3°, 32.8°, and 47.2°, which are indexed to the (111), (200), and (220) planes of cubic MgSe. When further discharged to 0.9 V (stage C), the peak at 12.8° shows decreased intensity, indicating that the as-formed Cu_2Se_y intermediate has participated in the further magnesiation reaction. After fully discharged to 0.2 V (stage D), the diffraction peaks of Cu_2Se_y disappear, and the peaks of MgSe show increased intensities; meanwhile, a strong new peak appears at 43.3°, corresponding to the (111) plane of metal Cu. When recharged again to 1.35 V (stage E), 1.48 V (stage F), and 2.2 V (stage G), the diffraction peaks of metal Cu and MgSe gradually disappear; the peaks of Cu_2Se_y emerge and then vanish again; finally, the peaks of final charge product $Cu_{2-x}Se$ reappear, indicating the reversibility of magnesiation/demagnesiation reactions. The electrochemical reactions of $Cu_{2-x}Se$ cathode during discharge–charge cycles can be described by the following equations:

$$2Cu_{2-x}Se + (2+xy-2y)Mg^{2+} + (2+xy-2y)e^- \rightleftharpoons (2-x)Cu_2Se_y + (2+xy-2y)MgSe \quad (1)$$

$$Cu_2Se_y + yMg^{2+} + 2ye^- \rightleftharpoons 2Cu + yMgSe \quad (2)$$

It is worth emphasizing that the Se^{2-} sub-lattices in MgSe are (fcc) lattices, which are the same as those in $Cu_{2-x}Se$. Moreover, the unite cell size of MgSe lattice (a = 0.546 nm) is similar to that of $Cu_{2-x}Se$ lattice (a = 0.573 nm). The same crystal structure and similar lattice sizes of the cathode material $Cu_{2-x}Se$

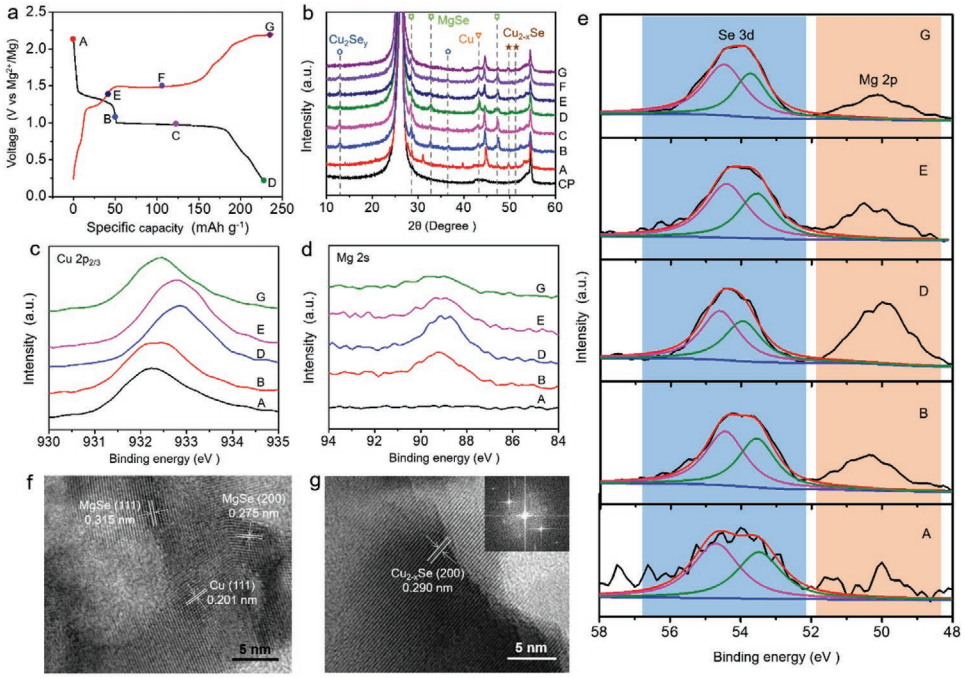

Figure 3. Ex situ structural and compositional characterizations of $Cu_{2-x}Se$ electrode at different discharge–charge states. a) Discharge–charge curves during the second cycle at the current density of 100 mA g^{-1}. The points labeled with A to G indicate the different discharge–charge states at which the ex situ X-ray powder diffraction (XRD) patterns and X-ray photoelectron spectroscopy (XPS) spectra were measured. b) Ex situ XRD patterns. c–e) ex situ XPS spectra at c) Cu 2p, d) Mg 2s, and e) Se 3d and Mg 2p energy levels. f,g) High-resolution transmission electron microscopy (HRTEM) images collected at the states of f) fully discharged to 0.2 V and g) fully recharged to 2.2 V.

and the discharge product MgSe are conducive to initiate the ionic displacement reaction. During discharging, Mg^{2+} ions diffuse into the Se^{2-} sub-lattices of $Cu_{2-x}Se$ to extrude the copper ions, accompanied with the generation of Cu_2Se_y and MgSe based on Se^{2-} sub-lattices, and finally resulted in the formation of metal Cu. This special magnesium storage process can ignore the unnecessary energy barrier for reconstructing the anion lattices, therefore it is obviously beneficial to improve the rate capability, structural integrity, and cycling stability of cathode material. At present, there are very few cathode materials based on ionic displacement mechanisms that can be used in RMBs (as summarized in Table S2, Supporting Information), and the $Cu_{2-x}Se$ nanoplates cathode exhibits very competitive electrochemical performances among them, including the cycle stability and rate capability. The magnesium storage performance of cubic-phase $Cu_{2-x}Se$ nanoplates is also superior to previously reported hexagonal-phase CuSe cathode based on traditional conversion reaction mechanism,[33] owing to the ion displacement mechanism occurs in the cubic-phase Se^{2-} based sub-lattices of $Cu_{2-x}Se$ nanoplates without causing lattice reconstruction and collapse.

To further investigate the mechanism of Mg^{2+} storage, ex situ XPS analysis of $Cu_{2-x}Se$ cathode at different discharge–charge states was also performed. When discharged from stage A to B, the high-resolution Cu 2p XPS spectra (Figure 3c) shows an upper shift of binding energy from 932.23 to 932.35 eV, suggesting the formation of Cu_2Se_y. Notably, at the fully discharged state (stage D), the Cu 2p peak shifts to the lower binding energy of 932.85 eV, representing the formation of metal Cu. During the charge process, the Cu 2p peak restores back to 932.35 eV at partially charged state (stage E) and finally reaches 932.25 eV at fully charged state (stage G), indicating the sequential reformation of Cu_2Se_y and then $Cu_{2-x}Se$, respectively. The Se 3d XPS spectra at different discharge–charge states (Figure 3e) indicate that the oxidation state of Se does not change, confirming that no Se and only Cu participates in the conversion reactions during the discharge–charge steps. Moreover, this result further demonstrates that the electrochemical redox processes of $Cu_{2-x}Se$ cathode are based on the ionic displacement mechanism. When discharged to 0.2 V (stage D), strong Mg 2s and Mg 2p peaks were observed at 89.0 and 50.0 eV (Figure 3d,e), respectively, and the intensities of these both peaks were significantly reduced at the fully charged state (stage G), indicating the reversible magnesiation/demagnesiation of $Cu_{2-x}Se$ cathode. The structural evolution of the cathode material during cycling is also characterized by HRTEM. At fully discharged state (stage D), the lattice fringes with spacings of 0.275 and 0.315 nm are indexed to the (200) and (111) planes of MgSe, respectively. The interplanar spacing of 0.201 nm is ascribed to the (111) planes of metal Cu (Figure 3f). When fully charged back to 2.2 V (stage G), the lattice fringes of $Cu_{2-x}Se$ (200) planes with the spacing of 0.290 nm are well recovered (Figure 3g), which is consistent with the results of XRD and XPS, confirming the good structural integrity and reversibility of $Cu_{2-x}Se$ cathode. In addition, ex situ EDX and ICP–OES were used to quantitatively evaluate the amount of Mg^{2+} cations inserted in $Cu_{2-x}Se$ cathode during cycling processes (Figure S8 and Table S1, Supporting Information). When partially discharged to 1.05 V (stage B), the atomic ratio of Mg/Cu increases to 0.38 as determined by ICP–OES (Table S1, Supporting Information), which is consistent to the

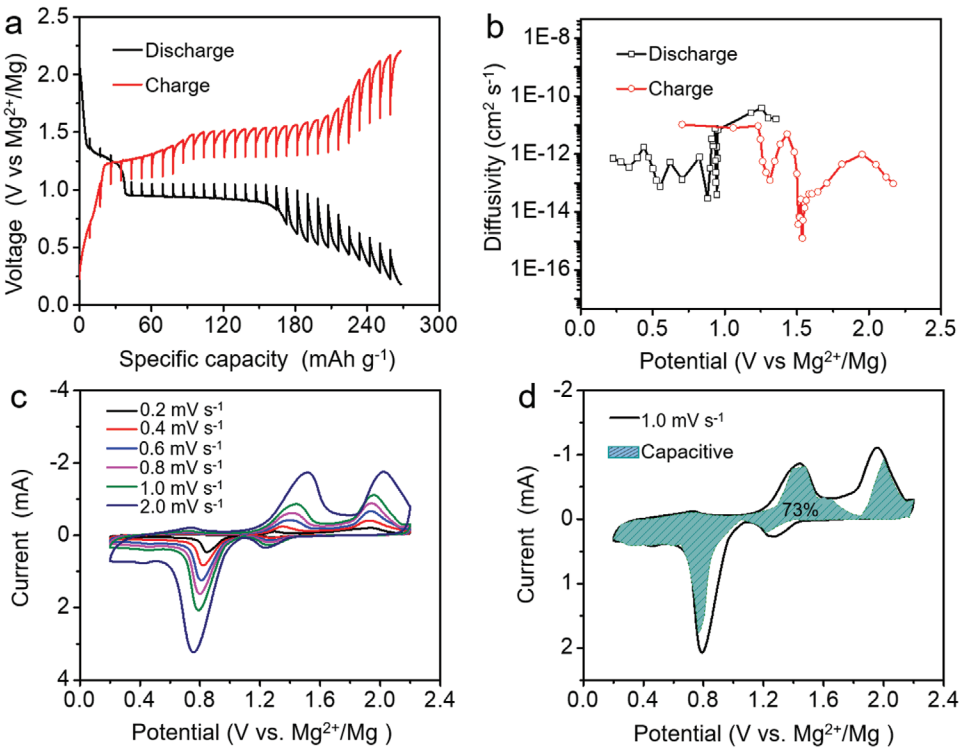

Figure 4. a) Discharge–charge curves of galvanostatic intermittent titration technique (GITT) test measured at the 10th cycle under a current density of 50 mA g^{-1} and b) corresponding diffusion coefficients of Mg^{2+} ions calculated from the GITT result. c) Cyclic voltammetry (CV) curves at different scan rates from 0.2 to 2.0 mV s^{-1}. d) The capacitive contribution measured at the scan rate of 1.0 mV s^{-1}.

EDX result (0.41, as shown in Figure S8a, Supporting Information). At fully discharged state (stage D), the Mg/Cu atomic ratio measured by ICP–OES further increases to 0.70 (or 0.74 as measured by EDX), indicating the formation of abundant MgSe by the ionic displacement. After fully charged back to 2.2 V (stage G), the Mg/Cu atomic ratio decreases back to 0.16 according to the ICP–OES result, comparable to the EDX result (0.21) and confirming the occurrence of demagnesiation process. The presence of residual Mg species is derived from a small quantity of electrolyte and Mg^{2+} ions remained in the $Cu_{2-x}Se$ cathode.

Galvanostatic intermittent titration technique (GITT) was used to evaluate the Mg^{2+} diffusive capability and the kinetics behavior of Mg^{2+} storage in the $Cu_{2-x}Se$ cathode (**Figure 4**a). The GITT test was conducted by applying a pulse current of 50 mA g^{-1} for 10 min followed by a rest time of 40 min. The diffusion coefficient of Mg^{2+} ions is calculated according to the Fick's second law.[34,35] The equation is as follows:

$$D_{Mg^{2+}} = \frac{4}{\pi}\left(\frac{iV_M}{z_A FS}\right)^2\left(\frac{\Delta E_s}{\Delta E_t}\right)^2 \quad (3)$$

Where i, V_M, Z_A, F, and S represent the pulse current, the molar volume of $Cu_{2-x}Se$, the charge number of Mg^{2+}, the Faraday constant, and the effective contact area of electrode/electrolyte, respectively. ΔE_s is the voltage change induced by the pulse current and ΔE_t is the voltage change induced by galvanostatic discharging–charging. As shown in Figure 4b, in spite of its double valence, the diffusion coefficient of Mg^{2+} ions is kept as high as 10^{-14}–10^{-11} cm^2 s^{-1} during the discharge–charge cycles. The fast Mg^{2+} migration rate provides a good explanation for the excellent rate performance of $Cu_{2-x}Se$ cathode. To further analyze the rate capability of $Cu_{2-x}Se$ electrode, CV curves were collected at different scan rates from 0.2 to 2.0 mV s^{-1} (Figure 4c). As displayed in Figure 4d, the capacitive contribution of $Cu_{2-x}Se$ electrode accounts for 73% of the total capacity at 1.0 mV s^{-1}, indicating that the Mg^{2+} storage in $Cu_{2-x}Se$ cathode is dominated by capacitive-controlled processes. As the scanning rate increases, the capacitive contribution to the total capacity becomes more prominent. Such a high capacitive contribution is beneficial to the charge transfer kinetics, leading to good rate performance.

3. Conclusion

In summary, we have successfully prepared cubic-phase $Cu_{2-x}Se$ nanoplates as a long-cycling cathode material for RMBs. A series of ex situ characterizations demonstrated that the reversible magnesium storage behavior of $Cu_{2-x}Se$ is based on an ionic displacement mechanism where the copper ions in the (fcc) Se^{2-} sub-lattices are displaced and extruded by Mg^{2+} ions without causing the collapse of Se^{2-} sub-lattices. The same face-centered cubic Se^{2-} sub-lattices and similar unit cell size of $Cu_{2-x}Se$ and MgSe greatly reduce the energy barrier for lattice reconstruction during the discharge–charge processes, which is

conducive to the rate capability, structural integrity, and cycling life of $Cu_{2-x}Se$ cathode. Therefore, the $Cu_{2-x}Se$ cathode exhibits an excellent rate performance (155 mAh g^{-1} at 1000 mA g^{-1}) and long cycling lifespan for over 500 cycles at 1000 mA g^{-1}. This finding demonstrates that the design of novel electrode materials based on reversible ion displacement mechanism is promising for the construction of advanced multivalent-ion secondary batteries.

Supporting Information

Supporting Information is available from the Wiley Online Library or from the author.

Acknowledgements

This work was supported by the National Key R&D Program (2017YFA0208200, 2016YFB0700600), the Projects of NSFC (22022505, 21872069, 51761135104), the Fundamental Research Funds for the Central Universities (0205-14380219), the Natural Science Foundation of Jiangsu Province (BK20180008), and the High-Level Innovation and Entrepreneurship Project of Jiangsu Province of China.

Conflict of Interest

The authors declare no conflict of interest.

Keywords

cathode materials, ionic displacement, multivalent-ion secondary batteries, nonstoichiometric cubic-phase copper selenide, rechargeable magnesium batteries

Received: November 4, 2020
Revised: November 29, 2020
Published online: December 18, 2020

[1] L. Lu, X. Han, J. Li, J. Hua, M. Ouyang, *J. Power Sources* **2013**, *226*, 272.
[2] K. Liu, Y. Liu, D. Lin, A. Pei, Y. Cui, *Sci. Adv.* **2018**, *4*, eaas9820.
[3] X. Xiang, K. Zhang, J. Chen, *Adv. Mater.* **2015**, *27*, 5343.
[4] J. Zhang, T. Liu, X. Cheng, M. Xia, R. Zheng, N. Peng, H. Yu, M. Shui, J. Shu, *Nano Energy* **2019**, *60*, 340.
[5] J. Muldoon, C. B. Bucur, T. Gregory, *Chem. Rev.* **2014**, *114*, 11683.
[6] A. Konarov, N. Voronina, J. H. Jo, Z. Bakenov, Y. K. Sun, S. T. Myung, *ACS Energy Lett.* **2018**, *3*, 2620.
[7] Y. Zhang, S. Liu, Y. Ji, J. Ma, H. Yu, *Adv. Mater.* **2018**, *30*, 1706310.
[8] Y. Wang, R. Chen, T. Chen, H. Lv, G. Zhu, L. Ma, C. Wang, Z. Jin, J. Liu, *Energy Storage Mater.* **2016**, *4*, 103.
[9] M. M. Huie, D. C. Bock, E. S. Takeuchi, A. C. Marschilok, K. J. Takeuchi, *Coord. Chem. Rev.* **2015**, *287*, 15.
[10] M. Mao, T. Gao, S. Hou, C. Wang, *Chem. Soc. Rev.* **2018**, *47*, 8804.
[11] Y. Liang, R. Feng, S. Yang, H. Ma, J. Liang, J. Chen, *Adv. Mater.* **2011**, *23*, 640.
[12] I. Shterenberg, M. Salama, Y. Gofer, E. Levi, D. Aurbach, *MRS Bull.* **2014**, *39*, 453.
[13] H. S. Kim, T. S. Arthur, G. D. Allred, J. Zajicek, J. G. Newman, A. E. Rodnyansky, A. G. Oliver, W. C. Boggess, J. Muldoon, *Nat. Commun.* **2011**, *2*, 427.
[14] L. Li, Y. Lu, Q. Zhang, S. Zhao, Z. Hu, S. L. Chou, *Small* **2019**, 1902767.
[15] Y. Cheng, Y. Shao, V. Raju, X. Ji, B. L. Mehdi, K. S. Han, M. H. Engelhard, G. Li, N. D. Browning, K. T. Mueller, J. Liu, *Adv. Funct. Mater.* **2016**, *26*, 3446.
[16] Z. Feng, J. Yang, Y. NuLi, J. Wang, *J. Power Sources* **2008**, *184*, 604.
[17] H. Dong, Y. Liang, O. Tutusaus, R. Mohtadi, Y. Zhang, F. Hao, Y. Yao, *Joule* **2019**, *3*, 782.
[18] D. Aurbach, Z. Lu, A. Schechter, Y. Gofer, H. Gizbar, R. Turgeman, Y. Cohen, M. Moshkovich, E. Levi, *Nature* **2000**, *407*, 724.
[19] J. Gong, P. K. Jain, *Nat. Commun.* **2019**, *10*, 3285.
[20] Y. Tashiro, K. Taniguchi, H. Miyasaka, *Chem. Lett.* **2017**, *46*, 1240.
[21] R. Zhou, Y. Huang, J. Zhou, H. Niu, L. Wan, Y. Li, J. Xu, J. Xu, *Dalton Trans.* **2018**, *47*, 16587.
[22] Y. Li, X. Sun, Z. Cheng, X. Xu, J. Pan, X. Yang, F. Tian, Y. Li, J. Yang, Y. Qian, *Energy Storage Mater.* **2019**, *22*, 275.
[23] S. C. Riha, D. C. Johnson, A. L. Prieto, *J. Am. Chem. Soc.* **2011**, *133*, 1383.
[24] H. Lin, M. Li, X. Yang, D. Yu, Y. Zeng, C. Wang, G. Chen, F. Du, *Adv. Energy Mater.* **2019**, *9*, 1900323.
[25] D. Wang, L. Wang, G. Liang, H. Li, Z. Liu, Z. Tang, J. Liang, C. Zhi, *ACS Nano* **2019**, *13*, 10643.
[26] Z. Zhao-Karger, R. Liu, W. Dai, Z. Li, T. Diemant, B. P. Vinayan, C. B. Minella, X. Yu, A. Manthiram, R. J. Behm, M. Ruben, M. Fichtner, *ACS Energy Lett.* **2018**, *3*, 2005.
[27] X. Xue, R. Chen, C. Yan, P. Zhao, Y. Hu, W. Kong, H. Lin, L. Wang, Z. Jin, *Adv. Energy Mater.* **2019**, *9*, 1900145.
[28] X. Li, T. Gao, F. Han, Z. Ma, X. Fan, S. Hou, N. Eidson, W. Li, C. Wang, *Adv. Energy Mater.* **2018**, *8*, 1701728.
[29] Y. Mao, G. Li, Y. Guo, Z. Li, C. Liang, X. Peng, Z. Lin, *Nat. Commun.* **2017**, *8*, 14628.
[30] D. S. Bin, X. J. Lin, Y. G. Sun, Y. S. Xu, K. Zhang, A. M. Cao, L. J. Wan, *J. Am. Chem. Soc.* **2018**, *140*, 7127.
[31] M. Okubo, E. Hosono, J. Kim, M. Enomoto, N. Kojima, T. Kudo, H. Zhou, I. Honma, *J. Am. Chem. Soc.* **2007**, *129*, 7444.
[32] Y. Shen, Y. Wang, Y. Miao, M. Yang, X. Zhao, X. Shen, *Adv. Mater.* **2019**, *32*, 1905524.
[33] S. Yang, F. Ji, Z. Wang, Y. Zhu, K. Hu, Y. Ouyang, R. Wang, X. Ma, C. Cao, *Electrochim. Acta* **2019**, *324*, 134864.
[34] Y. Xu, C. Zhang, M. Zhou, Q. Fu, C. Zhao, M. Wu, Y. Lei, *Nat. Commun.* **2018**, *9*, 1720.
[35] M. Mao, T. Gao, S. Hou, F. Wang, J. Chen, Z. Wei, X. Fan, X. Ji, J. Ma, C. Wang, *Nano Lett.* **2019**, *19*, 6665.